

Surface decorated coral-like magnetic BiFeO₃ with Au nanoparticles for effective sunlight photodegradation of 2,4-D and *E. coli* inactivation

Sze-Mun Lam^{a,b,c,*}, Zeeshan Haider Jaffari^{c,d}, Jin-Chung Sin^{a,b,e}, Honghu Zeng^{a,b,*}, Hua Lin^{a,b}, Haixiang Li^{a,b}, Abdul Rahman Mohamed^f, Ding-Quan Ng^d

^a College of Environmental Science and Engineering, Guilin University of Technology, Guilin 541004, China

^b Guangxi Key Laboratory of Theory and Technology for Environmental Pollution Control, Guilin University of Technology, Guilin 541004, China

^c Department of Environmental Engineering, Faculty of Engineering and Green Technology, Universiti Tunku Abdul Rahman, 31900 Kampar, Perak, Malaysia

^d Department of Environmental Engineering and Management, Chaoyang University of Technology, No. 168, Jifeng E. Rd, Wufeng District, Taichung 413310, Taiwan

^e Department of Petrochemical Engineering, Faculty of Engineering and Green Technology, Universiti Tunku Abdul Rahman, 31900 Kampar, Perak, Malaysia

^f School of Chemical Engineering, Universiti Sains Malaysia, Engineering Campus, 14300 Nibong Tebal, Pulau Pinang, Malaysia

ARTICLE INFO

Article history:

Received 28 November 2020

Received in revised form 7 January 2021

Accepted 9 January 2021

Available online 13 January 2021

Keywords:

BiFeO₃

Au

Magnetic

Composite

Photocatalysis

Antibacterial

ABSTRACT

In this report, gold nanoparticle-decorated on the coral-like magnetic BiFeO₃ (Au-BiFeO₃) composite has been successfully fabricated by facile two-steps hydrothermal technique. Incorporation of Au nanoparticles on the BiFeO₃ enabled effective harvesting sunlight for 2,4-dichlorophenoxyacetic acid (2,4-D) photodegradation and *Escherichia coli* (*E. coli*) inactivation on the heterojunction structures. The Au-BiFeO₃ composite exhibited ameliorated photoactivities toward pollutant photodegradation and bacterial disinfection as compared to that of bare BiFeO₃. The findings of these studies implied that decorating of Au on the coral-like BiFeO₃ can greatly delay the recombination process of the charge carriers produced by photon absorption and thus enhanced the photoactivity of the BiFeO₃. The possible photocatalytic mechanism was also postulated and supported by photoluminescence and electronic investigations. The radical trapping and electron spin resonance outcomes supported the role of the oxidative active species and its interaction for the degradation of 2,4-D. The intermediates responsible for the photodegradation have also been detected. Additionally, the prepared composite can be easily recovered through an external magnet and demonstrated good reusability within minimal release of deposited Au after six runs.

© 2021 Elsevier B.V. All rights reserved.

1. Introduction

The ever-increasing green environment and renewable energy demands have enthused considerable effort to explore new and sustainable technologies. Photocatalysis technology on semiconductor catalysts using abundant solar energy have aroused tremendous attention in the recent years owing to its tantalizing potential in the environmental and energy applications [1,2]. A plethora of catalysts, including titanium dioxide (TiO₂), zinc oxide (ZnO), tin dioxide (SnO₂), cerium dioxide (CeO₂) and cadmium sulfide (CdS) have been invented by the reasons of their particular optical, electronic and catalytic traits [3,4]. Nonetheless, the bare catalyst materials agonized from ultralow photoactivities and the limited photo-responding range greatly hampered their photoactivities in the visible region. Moreover, the difficulty in isolating the solid catalysts from the treated solution also rendered

their continuous wastewater treatment operations. Ergo, it was prime importance to develop magnetic catalysts, which enabled the integration of photocatalytic process with magnetic separation.

Among several magnetic-based materials, bismuth ferrite (BiFeO₃) is a unique and versatile because of its widespread of applications, including sensor, photovoltaic device, supercapacitor, electrocatalysis and photocatalysis [5]. BiFeO₃ is a multiferroic material with narrow band gap energy ~2.3 eV, demonstrating sufficient photocatalytic visible light response, high chemical stability and good magnetic separation ability [5,6]. It was well known that the fabrication technique and morphology were very crucial to the photoactivities of catalysts. So far, many BiFeO₃ morphological structures have been revealed, such as wire, plate, spherical-like, sheet, cube and bowl array [7–10]. The morphological alteration can enhance light harvesting and provided larger interface contacting area with electrolyte for the photocatalysis [11,12]. However, the high surface-charge recombination rate of the pure BiFeO₃ still restricted the utilization of charge carriers and thus compromising its photoactivity.

On the other hand, some researchers have highlighted that adequate noble metal (Ag, Pd, Pt and so on) co-catalysts decoration on the catalyst

* Corresponding author at: College of Environmental Science and Engineering, Guilin University of Technology, Guilin 541004, China.

E-mail addresses: lamsm@utar.edu.my (S.-M. Lam), zenghonghu@glut.edu.cn (H. Zeng).

material surface were an effective strategy to enhance the photocatalytic performance. It has been revealed that noble metal cocatalysts can serve as electron reservoirs to suppress the recombination of charge carrier of the adjacent catalysts as well as provided more active catalytic sites [12]. Moreover, such “electron reservoirs” approach is able to strengthen the electron density of noble metals and raised the intrinsic photoactivity of catalysts, which can make them act as better candidates for visible light driven applications [13]. Among gold (Au) has always been one of the broadly explored materials in variety areas of research owing to its excellent optical and electrical properties. The Au nanoparticle demonstrated good visible light absorption because of the interband transition (*5d* band to *6sp* band) [14].

As the wastewater from agricultural and industrial activities not only comprised the waste pollutants, but also several microorganisms which can cause environmental issues and human health, researchers have always been keen to explore multifunctional materials that can be exploited for more than one application. In this report, the gold-decorated on the coral-like magnetic BiFeO₃ (Au-BiFeO₃) composites have been fabricated by simple two-steps hydrothermal method. The as-fabricated composite with coral-like structure displayed outstanding ability for sunlight photodegradation of 2,4-dichlorophenoxyacetic acid (2,4-D). 2,4-D as a typical herbicide compound which was widely used in agricultural production and posing a significant adverse effect [4]. The incorporation of Au nanoparticle on the coral-like BiFeO₃ also demonstrated a good antibacterial activity toward *Escherichia coli* (*E. coli*). The active radicals during photodegradation process were also assessed by radical trapping test and the electron spin resonance (ESR) technique and thus the photocatalytic mechanism was postulated.

2. Experimental section

2.1. Reagents

Iron nitrate (Fe(NO₃)₃·9H₂O, 98%), methanol (98%), tetrachlorogold (III)-saurehydrat (HAuCl₄, 99%) and nitric acid (HNO₃, 65%) were obtained from ChemSoln. Bismuth nitrate (Bi(NO₃)₃·5H₂O, 98%) and 2,4-dichlorophenoxyacetic acid (2,4-D, 97%) was acquired from Merck and Sigma-Aldrich, respectively. Potassium hydroxide (KOH, 85%) and urea (99.5%) were purchased from R & M Chemicals. All reagents were utilized as received and deionized water (Milipore System, 18.2 Ω) was utilized as solvent.

2.2. Synthesis of Au-BiFeO₃ composites

In a typical synthesis of bare BiFeO₃, 0.006 mol of Bi(NO₃)₃·5H₂O, 0.006 mol of Fe(NO₃)₃·9H₂O, 0.1 mol of urea and 2 mL of HNO₃ were dissolved in deionized water (20 mL) under stirring until completely dissolved. After that, the mixed solution was added in the KOH (10 M). The mixture was then shifted into a Teflon-lined autoclave reactor and heated at 125 °C for 15 h. After cooling down to room temperature, the obtained product was centrifuged, washed with ethanol and deionized water and dried in an oven at 80 °C.

The Au-BiFeO₃ composites were prepared using a hydrothermal technique in the presence of HAuCl₄. In this experiment, a fixed amount of HAuCl₄ in methanol (40 mL) was sonicated in ultrasonication bath (40 kHz/100 W) for 20 min. Subsequently, 1 g of BiFeO₃ was inserted in the solution and further sonicated for 30 min. After that, the solution was moved into a Teflon-lined autoclave reactor and heated at 100 °C for 4 h. The autoclave was then allowed to cool down naturally. The orange precipitation of Au-BiFeO₃ was collected by filtration, washed and oven dried at 80 °C for overnight. A schematic diagram of Au-BiFeO₃ composites synthesis using a two-steps hydrothermal technique is revealed in Scheme 1.

2.3. Material characterization

The surface morphology of bare BiFeO₃ and Au-BiFeO₃ samples were captured using a field-emission scanning electron microscopy (FESEM, Quanta FEG 450), transmission electron microscopy (TEM, Tecnai G220), high-resolution transmission electron microscopy (HRTEM, JEM-200 CX). Crystalline structure was measured using an X-ray diffraction (XRD, Philips PW 1820) diffractometer. The elemental composition of the samples was assessed using an energy dispersive X-ray (EDX) instrument coupled with a FESEM. The X-ray photoelectron spectra (XPS) was examined using a Thermo Escalab 250Xi spectrometer. The N₂ physisorption isotherm was recorded using a Brunauer Emmett Teller analyzer (BET, ASAP 2020 M). The diffuse reflectance spectra of bare BiFeO₃ and Au-BiFeO₃ samples were taken using a Perkin Elmer L35 spectrophotometer. The photoluminescence (PL) spectra of as-prepared materials were recorded using a Perkin Elmer S55 spectrophotometer. The magnetic hysteresis (M-H) loops of the samples were determined using a MicroSense 10 Mark II analyzer. The zeta potential of the Au-BiFeO₃ composite was recorded using a Malvern Zetasizer Nano-Z.

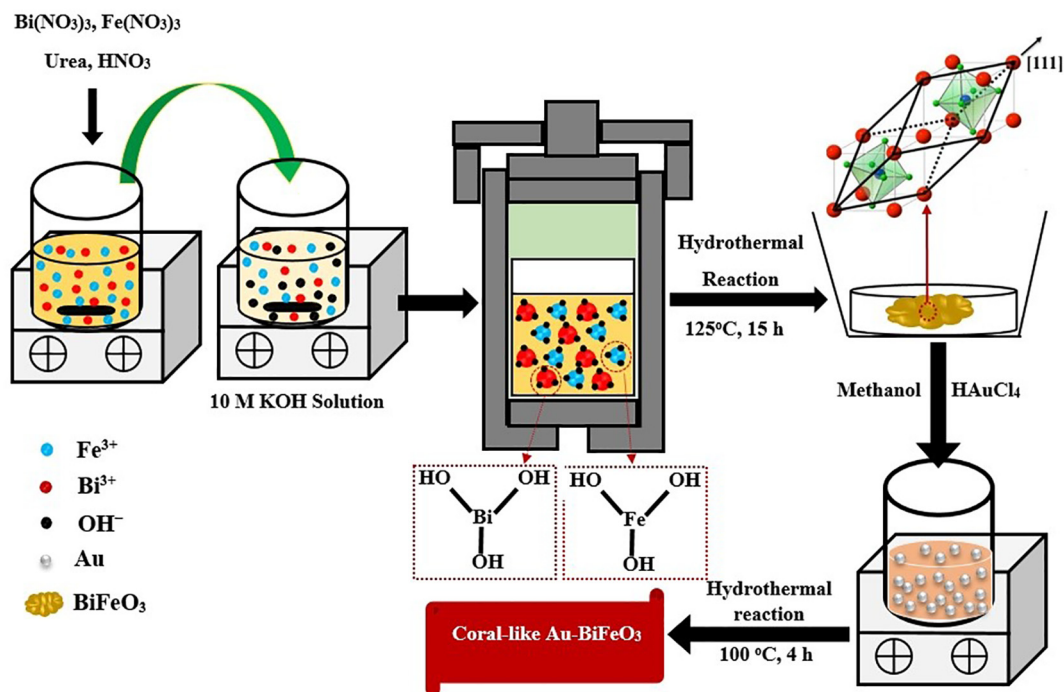
2.4. Photoelectrochemical measurements

Photoelectrochemical analyses on the samples were investigated using an electrochemical workstation (*Gamry Interface 1000*) in a three-electrode system containing 0.5 M sodium sulfate as an electrolyte solution. Samples were coated on fluorinated tin oxide (FTO) glass, which acted as a working electrode. Ag/AgCl and platinum wire were applied as a reference electrode and a counter electrode, respectively. Transient photocurrent response was investigated with 30 s off/on cycles with a bias potential of 0.4 V vs Ag/AgCl. The Nyquist plot was performed in the frequency from 0.1 to 10⁴ Hz and linear sweep voltammetry (LSV) was executed at 50 mV/s scanning rate.

2.5. 2,4-D photodegradation test

The photoactivity of the composite was investigated in a designated photoreactor setup comprising light source and two mounted fans in an acrylic black enclosure. Typically, 1 g/L of the catalyst was placed in a 100 mL of 20 mg/L 2,4-D solution. The test was first conducted under dark condition for 30 min to achieve adsorption-desorption equilibrium between the solids and solution under magnetic stirring. The solution was then placed under sunlight with the measured light intensity of 865.7 W/m². Throughout the test, the air with a flow rate of 2 mL/min was constantly bubbled in the solution. At different time intervals, the sample solution was determined using a high performance liquid chromatography (HPLC, Perkin Elmer Series 200) equipped with a C18 column (150 mm × 4.6 mm × 5 μm). The wavelength of UV detector was fixed at 280 nm and a solvent mixture of acetonitrile, acetic acid and water in the ratio of 69:1:30 (v/v) with a flow rate of 1 mL/min. The chemical oxygen demand (COD) of samples was tested using a UV-vis Hach DR6000 spectrophotometer. The Cl⁻ ions left in the solution was monitored using a Metrohm 792 Basic Ion Chromatography (IC) coupled with a Metrosep C4 column. In order to ascertain the active species that influence the 2,4-D degradation, 1 mM of capturing agents, including isopropanol, benzoquinone, potassium iodide and catalase were adopted to scavenge hydroxyl (•OH) radical, superanion oxide (•O₂⁻) radical, hole (h⁺) and hydrogen peroxide (H₂O₂), respectively. Additionally, electron spin resonance (ESR, Bruker EMX plus) with 5,5-dimethyl-1-pyridine N-oxide (DMPO) as a quencher agent was used to further confirm the •OH radical.

Recycling test of the Au-BiFeO₃ composite was performed over six cyclic runs. The Au-BiFeO₃ composite in each run was centrifuged, cleaned with deionized water and dried at 120 °C for 4 h. Afterwards, the dried sample was again inserted in fresh 2,4-D solution for the next run. The dissolved Fe³⁺ and Au⁰ in the treated solution were



Scheme 1. Schematic diagram of the synthesis of Au-BiFeO₃ composites using a two-steps hydrothermal process.

analyzed via an inductively coupled plasma mass spectroscopy (ICP-MS, Perkin Elmer AA-6650). All tests were at least duplicated and the average values were presented with standard deviation error bars.

2.6. Antibacterial assay

Minimum inhibitory concentration (MIC) was defined as the minimum quantity of solid samples which capable to completely inhibit the visible growth of bacteria. The MIC of *Escherichia coli* (*E. coli* bacteria (ATCC 25922) in the presence of bare BiFeO₃ and Au-BiFeO₃ samples was assessed in the current study [15]. All the glassware was sterilized by autoclaving at 120 °C for 20 min, and the antibacterial activity was carried out under sterile conditions. The Au-BiFeO₃ composite was serially diluted to achieve a 96-well plate. These wells were then inoculated with bacterial concentration of 5×10^5 CFU/mL and the plates were incubated at 37 °C for 24 h before examining the bacterial concentrations.

3. Results and discussion

3.1. Physicochemical characteristics of Au-BiFeO₃

The morphology and the detailed structures of the as-fabricated samples were analyzed by FESEM, TEM and HRTEM as presented in Fig. 1. It can be seen in Fig. 1a that the bare BiFeO₃ powders demonstrated coral-like morphologies which were interconnected as networks with particle sizes of approximately 110–140 nm. Apparently, composite in Fig. 1b–e showed similar morphological features as those observed in the bare BiFeO₃. Nonetheless, the difference between these samples was that a small amount of Au nanoparticles was deposited on the BiFeO₃ surfaces. The distribution of Au nanoparticles on coral-like BiFeO₃ surfaces observed from TEM image (Fig. 1f) further confirmed by the realization of Au-BiFeO₃ heterostructures formation. The HRTEM image in Fig. 1g displayed the lattice fringes with 0.27 nm

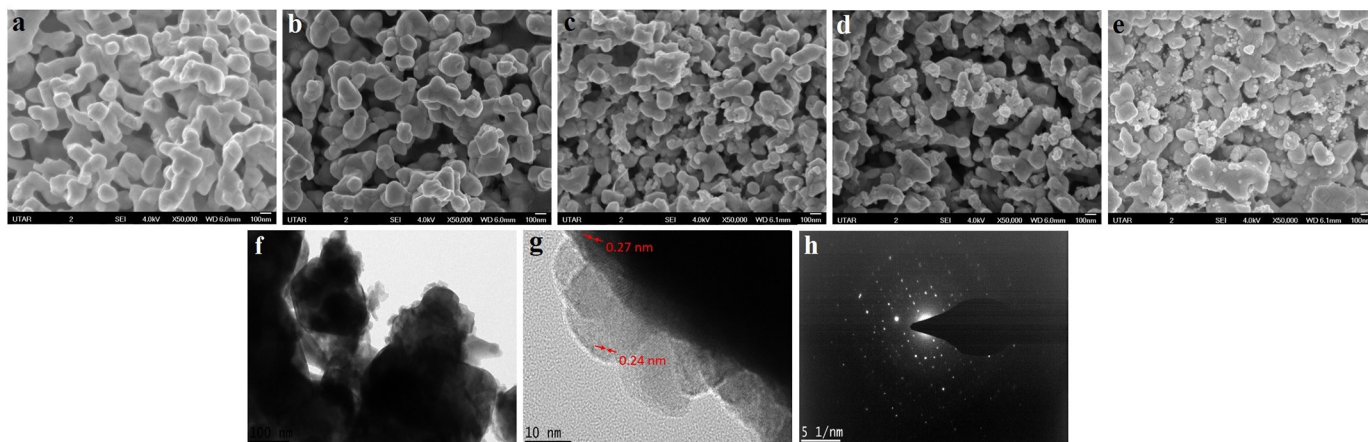


Fig. 1. FESEM images of (a) bare BiFeO₃, Au-BiFeO₃ decorated at different Au loadings of (b) 0.25 wt%, (c) 0.5 wt%, (d) 1 wt%, (e) 2 wt%, (f) TEM image, (g) HRTEM image and (f) SAED pattern of 1 wt% Au-BiFeO₃.

and 0.24 nm can be assigned to d spacings of (110) of rhombohedral perovskite BiFeO_3 and (011) planes of Au, respectively [16,17]. Many diffraction rings in the SAED pattern in Fig. 1h also revealed the polycrystalline nature of Au- BiFeO_3 composite.

The crystalline structures and elemental composition of the as-fabricated catalysts have been studied by XRD and EDX, respectively. As shown in Fig. 2a, bare BiFeO_3 displayed well-defined peaks occurring at $2\theta = 22.6^\circ, 32.2^\circ, 32.4^\circ, 39.9^\circ, 45.9^\circ, 51.8^\circ, 52.4^\circ, 56.6^\circ, 58.2^\circ, 67.2^\circ, 67.8^\circ, 71.1^\circ, 71.9^\circ, 76.5^\circ$ and 76.9° , which can be respectively indexed to the (012), (104), (110), (202), (024), (116), (122), (018), (214), (208), (212), (131), (036), (128) and (134) diffraction planes of rhombohedral phase with space group $R3c$ [JCPDS NO. 86–1518] [8,9]. After incorporation of Au into BiFeO_3 , three small peaks at 38.4° (111), 44.3° (200) and 64.5° (220) corresponded to the face-centered cubic Au [JCPDS NO. 65–2870] appeared distinctly, deducing the effective combination of Au with BiFeO_3 [18]. No other new peaks can be seen in all the obtained samples, suggesting the high purity of the Au- BiFeO_3 composites. Additionally, EDX in Fig. 2b presents also gold, bismuth, iron and oxygen as the major peaks. The EDX elemental mapping is shown in Fig. 2c–f.

The chemical states of the samples have also been evaluated by XPS. The high resolution XPS spectra of Bi 4f, Fe 2p, O 1s, and Au 4f for bare BiFeO_3 and Au- BiFeO_3 are exhibited in Fig. 3. In the high resolution XPS spectrum of Au 4f peaks (Fig. 3a), the doublet peaks for Au 4f_{7/2} and Au 4f_{5/2} were positioned at 83.3 and 87.3 eV, respectively, indicating that the existence of Au cocatalyst present in the composite [19,20]. Two XPS peaks appeared at 158.4 and 163.7 eV associated with Bi 4f_{7/2} and Bi 4f_{5/2}, respectively, validating that the chemical state of Bi was trivalent oxidation state (Fig. 3b) [21]. The typical high resolution Fe 2p spectrum in Fig. 3c illustrated doublet peaks at 710.8 and 724.2 eV corresponding to the Fe 2p_{3/2} and Fe 2p_{1/2}, respectively and a satellite peak observed at 718.8 eV can be viewed as the Fe element in the form of Fe^{3+} [22]. The O 1s spectrum in Fig. 3d can be resolved into two peaks located at 529.6 and 530.9 eV, corresponding to the metal-oxygen bond and chemisorbed oxygen, respectively [23].

Additionally, it was well nothing that all signals of Bi 4p, Fe 2p and O 1s in the composite were slightly shifted to higher energy level as compared to that of bare BiFeO_3 . These small shift in the binding energy demonstrated some degree of electron transfer between the Au and BiFeO_3 and intense interaction within the composites [24].

To examine the surface area and pore size distribution, N_2 adsorption-desorption isotherms of the bare BiFeO_3 and composite were carried out. As depicted in Fig. 4a, both the samples displayed typical type IV adsorption isotherms associated with the mesoporous structures. The BET surface area of Au- BiFeO_3 was $19.6 \text{ m}^2/\text{g}$ higher than that of $11.2 \text{ m}^2/\text{g}$ of bare BiFeO_3 . The total pore volume and pore size distribution for both samples was determined from the desorption isotherms from BJH plot are shown in Fig. 4b. The total pore volume and mean pore size diameter of bare BiFeO_3 was estimated to be $0.0028 \text{ cm}^3/\text{g}$ and 21.6 nm, respectively. After decoration with Au nanoparticles, the total pore volume increased to $0.0043 \text{ cm}^3/\text{g}$ and mean pore size diameter decreased to 17.1 nm. It should be noted that the high surface area of Au- BiFeO_3 afforded more active sites for pollutant molecules and expected to increase the photocatalytic oxidation efficiency.

3.2. Optical and electrochemical properties

The optical absorption property of Au- BiFeO_3 composite was studied using UV-vis DRS analysis (Fig. 5a). Compared with bare BiFeO_3 , the Au- BiFeO_3 composites displayed enhanced visible light absorbance around the 500–800 nm. Moreover, this absorption characteristic improved significantly with Au loadings in the heterojunction composites. Fig. 5b depicts the Kubelka-Munk (K-M) plots according to the obtained UV-vis DRS data. The optical band gap (E_g) of bare BiFeO_3 and Au- BiFeO_3 composite prepared at 1.0 wt% were measured to be 2.60 and 2.35 eV, respectively. The declined E_g value suggested that the Au- BiFeO_3 can afford strong ability to harvest the full solar spectrum for the photo-oxidation process. The conduction band (CB) and valance band (VB) potential of BiFeO_3 can be determined as follows [25,26].

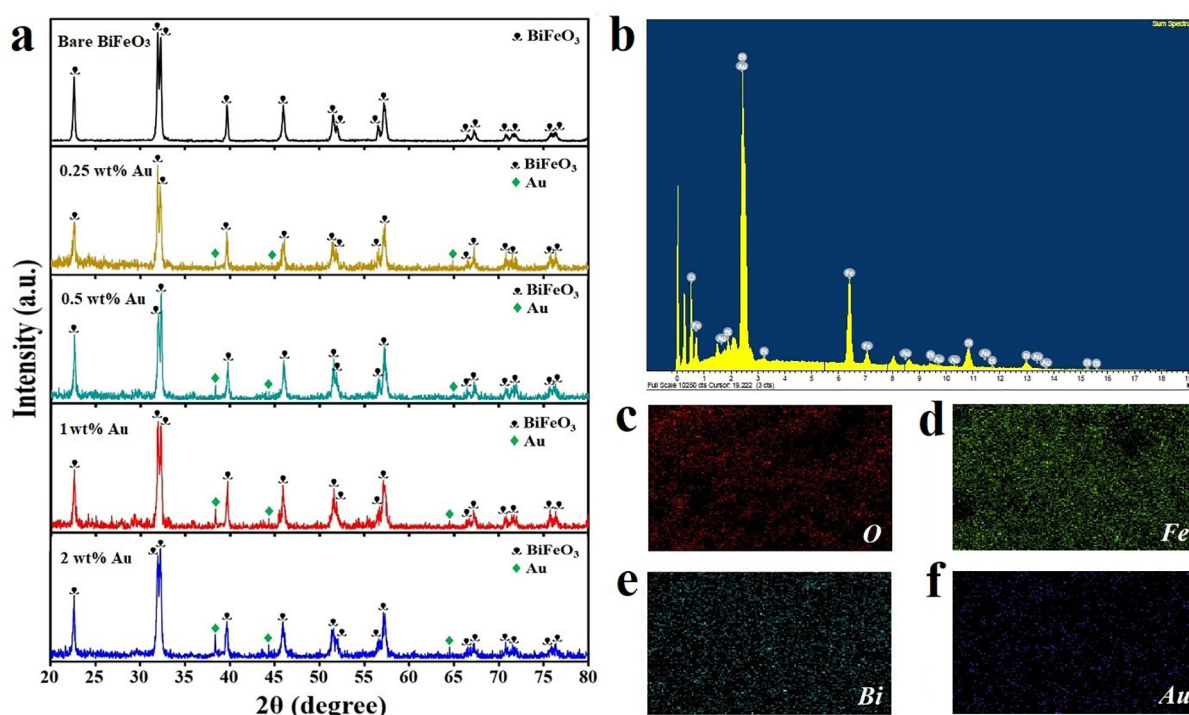


Fig. 2. XRD patterns of (a) bare BiFeO_3 , and Au- BiFeO_3 composites prepared at different Au loadings, (b) EDX spectrum of Au- BiFeO_3 and (c–f) EDX elemental mapping validating Au- BiFeO_3 .

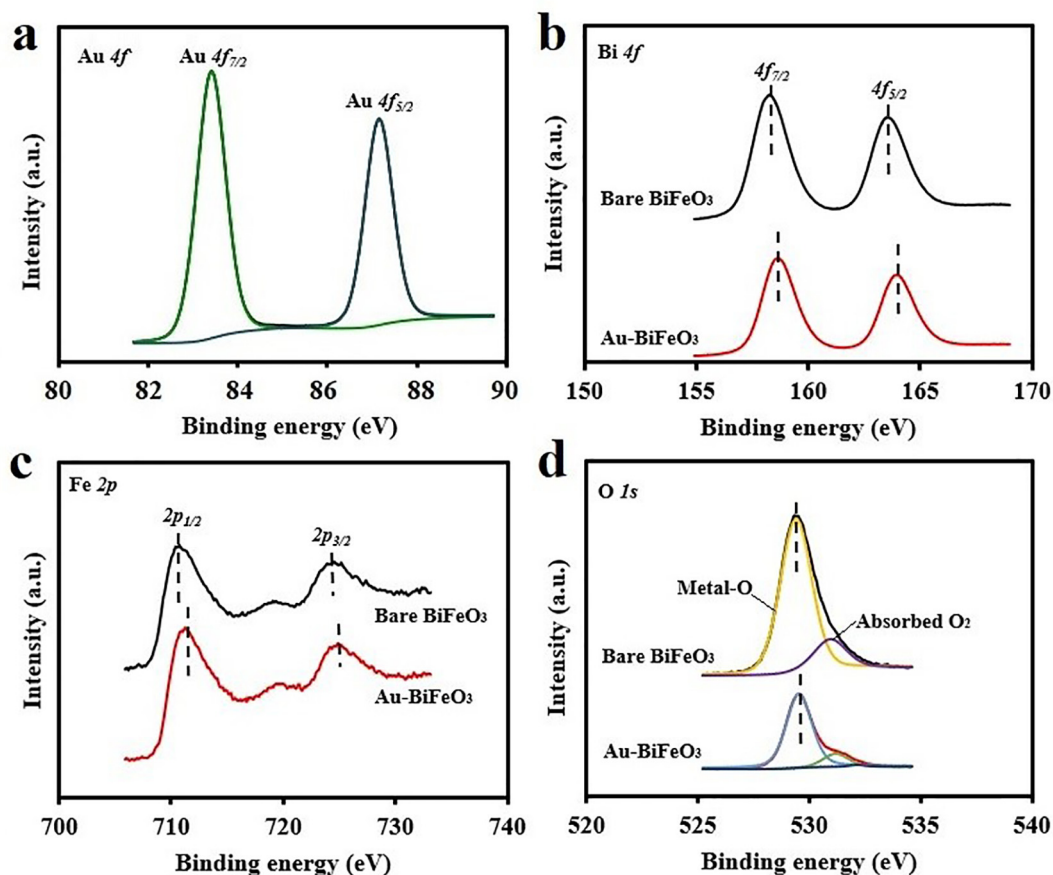


Fig. 3. High resolution XPS spectra of Au-BiFeO₃ composite (a) Au 4f, (b) Bi 4f, (c) Fe 2p and (d) O 1 s.

$$E_{VB} = X - E^e + 0.5E_g \quad (1)$$

$$E_{CB} = E_{VB} - E_g \quad (2)$$

where, E_{CB} is the conduction band potential, E_{VB} is the valance band potential, E^e is the free electron energy on hydrogen scale (4.5 eV), band gap energy (E_g) of BiFeO₃ (eV) and X is the Pearson absolute electronegativity. This X value can be determined as show in Eq. (3) [27,28].

$$X(AmBnCl) = \frac{(m+n+1)}{\sqrt{X_A^m X_B^n X_C^1}} \quad (3)$$

As for BiFeO₃, the absolute electronegativities of Bi, Fe, and O were 4.69 eV, 4.06 eV and 7.54 eV, respectively. Hence, from the aforementioned formula, the computed $X(\text{BiFeO}_3)$ was 6.06 eV. This value was fitted in the Eqs. (1) and (2), the calculated E_{VB} and E_{CB} of BiFeO₃ was 2.86 and 0.26 eV, respectively.

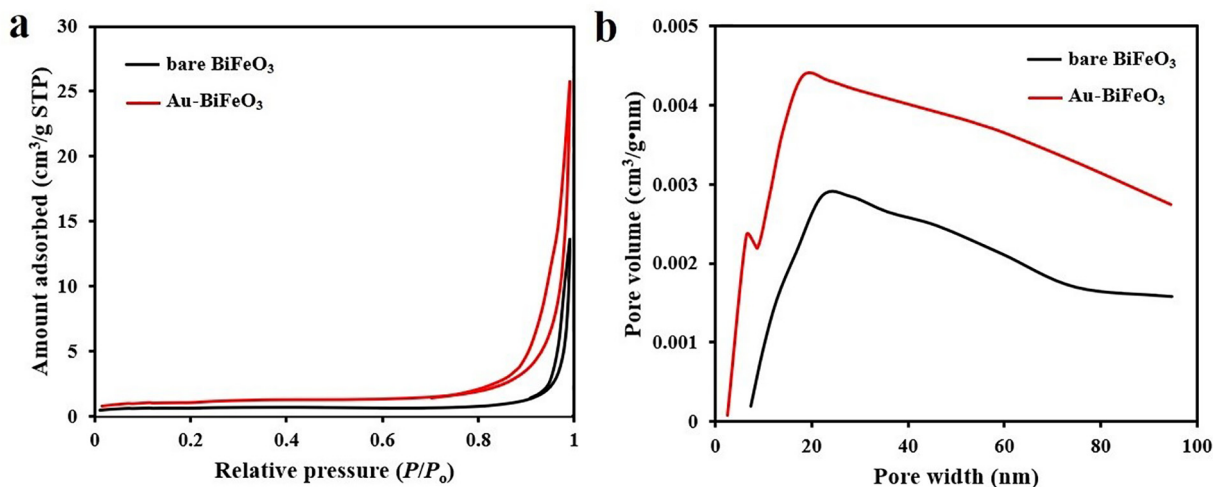


Fig. 4. (a) N₂ adsorption-desorption isotherm and (b) variations in total pore volume and pore size diameter of the bare BiFeO₃ and Au-BiFeO₃.

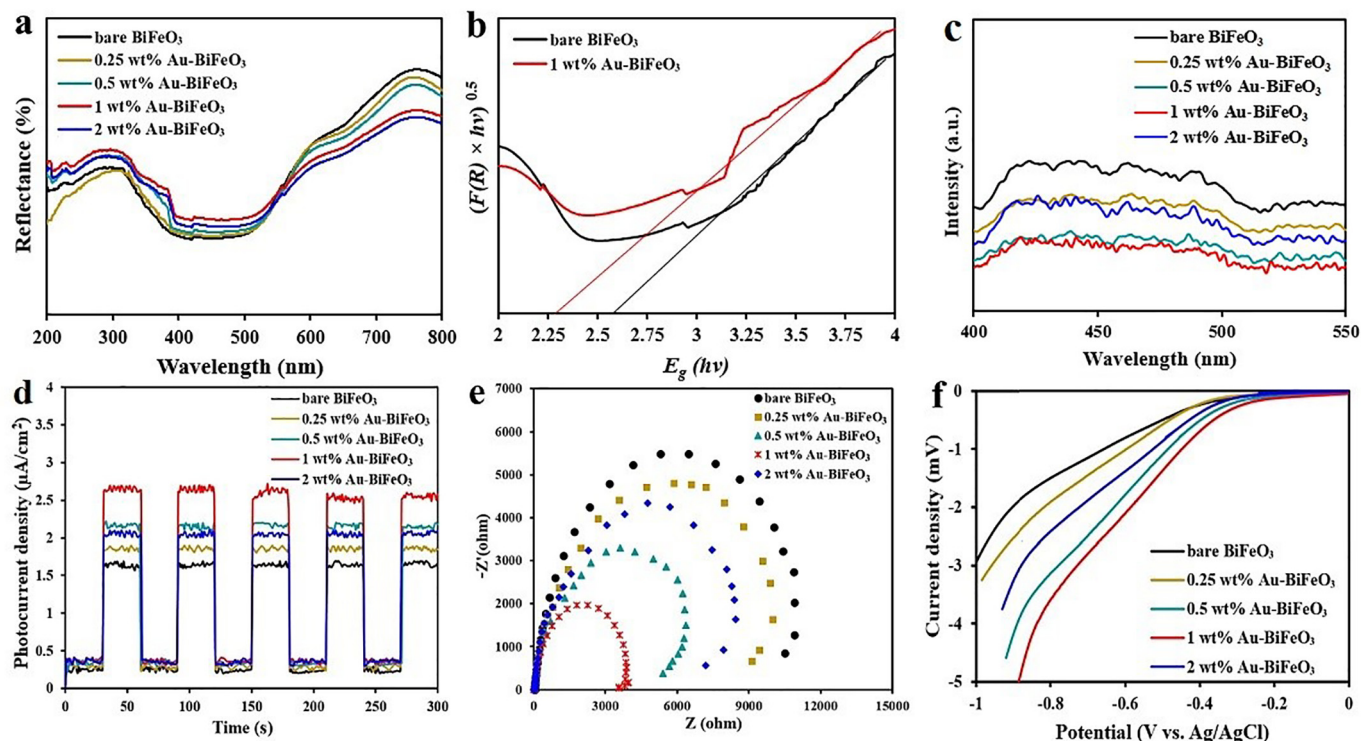


Fig. 5. (a) UV-Vis DRS spectra, (b) corresponding K-M plots of bare BiFeO₃ and Au-BiFeO₃ composites, (c) PL spectra, (d) transient photocurrent responses, (e) EIS Nyquist plots and (f) LSV curves of bare BiFeO₃ and Au-BiFeO₃ composites with various Au loadings.

The PL analysis is a method used to assess the separation and transfer dynamics of photogenerated electrons and holes. Fig. 5c presents the PL spectra of Au-BiFeO₃ composite materials together with the bare BiFeO₃. The intense PL intensity of bare BiFeO₃ indicated the rapid recombination of excitons. In contrast, PL spectrum of 1.0 wt% Au-BiFeO₃ composite was entirely quenched because of its low recombination rate of the charge carriers, which was a crucial factor in the photocatalytic reactions. In order to further examine the recombination rate of excitons, electrochemical studies, including transient photocurrent response, EIS Nyquist and LSV measurements of bare BiFeO₃ and Au-BiFeO₃ composite was performed. The transient photocurrent response was applied to investigate the mobility of photogenerated charge carrier under light irradiation. Fig. 5d depicts the transient photocurrent responses with light on and off cycles using the bare BiFeO₃ and Au-BiFeO₃ composites. A substantial enhancement in the transient photocurrent response of 1 wt% Au-BiFeO₃ composite inferred that greater photogenerated electron-hole separation efficiency and higher mobility in comparison with the bare BiFeO₃ [29,30]. The EIS Nyquist plot was executed to measure the interfacial charge transfer resistance in the prepared samples. Fig. 5e illustrates that 1 wt% Au-BiFeO₃ composite demonstrated the lowest arc radius, signifying the excellent charge separation and lowest charge transfer resistance at the interface among the sample. Additionally, the LSV analysis was also conducted to further confirm the photoelectrochemical performance of the catalyst materials. As displayed in Fig. 5f, the highest current density and lowest overpotential of 1 wt% Au-BiFeO₃ composite obviously indicated that it can more appropriately improve the separation and transfer of charge carriers than those of the remaining catalysts. These ameliorated optical absorption and improved electrochemical features of the Au-BiFeO₃ composite materials deduced that they can be adopted as an effective sunlight-activated catalyst.

3.3. Sunlight photodegradation of 2,4-D using Au-BiFeO₃ composites

Fig. 6a shows the photoactivities of bare BiFeO₃ and Au-BiFeO₃ composites with various Au loadings for the sunlight degradation of 2,4-D. It

can be seen that the 2,4-D concentration hardly changed under both the dark and photolysis conditions. After the introduction of bare BiFeO₃, about 50% 2,4-D was degraded within 120 min irradiation. For the Au-BiFeO₃ composites, 1.0 wt% Au-BiFeO₃ composite exhibited the optimum photoactivity with the degradation efficiency as high as 98.5%. This finding conveyed the critical role of Au cocatalyst in enhancing the photoactivity of coral-like BiFeO₃. When comparing the different Au loadings in the composites, the photoactivities of the Au-BiFeO₃ composites were first rose up and then restrained with the increasing loadings of Au. The reasons could be attributed to the Au nanoparticles at the Au-BiFeO₃ interface can prevent the photoexcited electrons to return the BiFeO₃ surface and prolonged the charge carrier recombination time [31]. On the contrary, the decline photoactivity could be considered to the photons scattering effect by Au and the blocked the incident light absorption by the BiFeO₃ [32,33]. Thus, the loading amount of Au was kept a desirable balance between the BiFeO₃ and Au cocatalyst. In order to quantitatively check the catalyst activity, the photodegradation kinetics of 2,4-D was also studied. Considering the 2,4-D low concentration (20 mg/L) used in this study, the pseudo-first-order kinetic model was chosen. The kinetic curves of 2,4-D photodegradation under sunlight irradiation are illustrated in Fig. 6b. Besides, the histogram kinetic constant in the inset of Fig. 6b manifested that the 1.0 wt% Au-BiFeO₃ sample (0.0283 min⁻¹) was higher those of bare BiFeO₃ and other Au-BiFeO₃ composites.

3.3.1. Influence of solution pH

Photodegradation rate was intensely influenced by the solution pH as the pH variation can affect 2,4-D molecules adsorption on the Au-BiFeO₃ catalyst surface. To scrutinize the influence of solution pH on the photocatalytic efficiency, four different pH values at 3, 5, 7 and 9 was prepared and other experiment conditions at initial 2,4-D concentration of 20 mg/L and catalyst loading of 1 g/L were fixed and the findings are presented in Fig. 7a. As can be seen, the pH variations were effective in the 2,4-D photodegradation efficiency wherein with the solution pH reduction the photodegradation efficiency increased and pH 2 was the highest photodegradation efficiency. Semiconductor metal

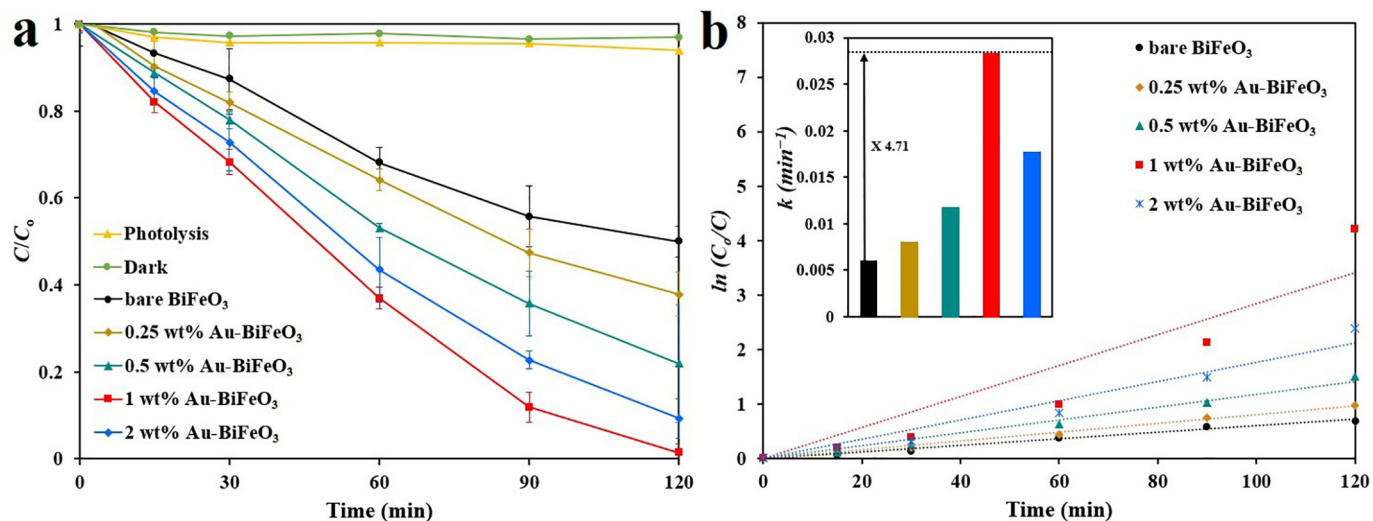


Fig. 6. (a) Photodegradation of 2,4-D and (b) pseudo-first-order reaction kinetics curves over Au- BiFeO_3 composites under sunlight irradiation. Inset of (b) the histogram of kinetic rate constants for 2,4-D photodegradation.

oxide typically displayed an amphoteric behavior, which it can affect the surface zero-point charge (zpc) characteristic of the catalyst when the reaction occurred on the semiconductor surface. The zpc of Au- BiFeO_3 composite was extrapolated to be pH 2 (as recorded in Fig. 7b). Hence, the surface of Au- BiFeO_3 catalyst was positively charged at $\text{pH} < \text{pH}_{\text{zpc}}$, while negatively charged at $\text{pH} > \text{pH}_{\text{zpc}}$. Additionally, the electric charge property of pollutant was also observed to serve as a pivotal role on the photodegradation process. The 2,4-D has a pK_a of 2.98. It was preferably presented in the molecular form rather than ionic in the alkaline condition [4]. At low pH, a strong adsorption of the 2,4-D on the Au- BiFeO_3 particles was found due to the electrostatic reactions of the negatively charged catalyst with the pollutant. While in the alkaline condition, the 2,4-D molecules were in ionic form, their adsorption were expected to be affected by the negative surface charge of Au- BiFeO_3 . Therefore, owing to Coulombic repulsion, the 2,4-D were hardly adsorbed.

3.3.2. Influence of catalyst loading

Catalyst loading was one of the crucial factors than can govern the photodegradation rate of 2,4-D. Fig. 7b illustrates the influence of catalyst loading on the 2,4-D photodegradation using Au- BiFeO_3 examined at the range of 0.5–2 g/L at the initial 2,4-D concentration of 20 mg/L and optimal pH 3. As can be seen, with addition of the catalyst loadings to the initial photodegradation process, it can increase up to a specific

level and thereafter, the photodegradation rate happened at a lower rate. At a low catalyst loading, sunlight transfer at a higher rate to the solution. This phenomenon caused the 2,4-D photodegradation increased since the increment of the catalyst loadings promoted the contact and active sites between the catalysts and pollutants. However, when the catalyst was overloaded, the increased solution turbidity and limited light penetration into the suspension resulted in the decrease in the photoactivity. Therefore, 1 g/L was selected as the optimal loading.

3.4. Intermediate identification and possible photodegradation pathway

The photodegradation of 2,4-D over 1.0 wt% Au- BiFeO_3 composite was studied by evaluating the mixture solution at different treatment periods through HPLC technique. Four aromatic intermediates, namely 2,4-dichlorophenol (P1) (Retention time (RT) = 2.75 min), 4-chlorophenol (P2) (RT = 2.32 min), chlorobenzoquinone (P3) (RT = 2.10 min), and phenol (P4) (RT = 1.92 min) were identified (Fig. 8a) after compared with the standard chemicals. These intermediates were started to display in the middle of the reaction and progressively disappeared when the irradiation time prolonged. At the end of the test, none of the intermediate was found in the HPLC profiles. The degree of mineralization of 2,4-D was monitored by COD analysis, while the ion chromatography (IC) assay was employed to analyze the concentration of free chloride (Cl^-) ion in the solution (Fig. 8b). The

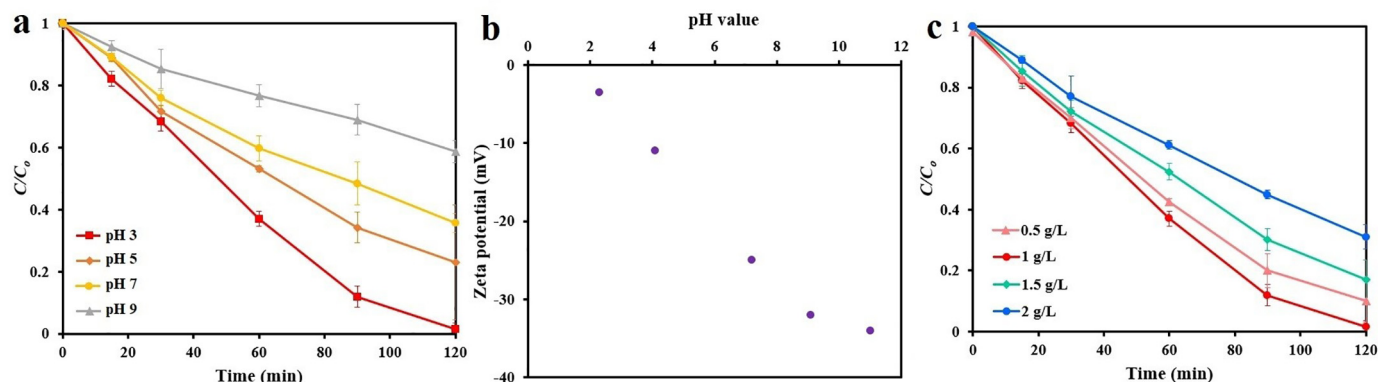


Fig. 7. (a) Influence of pH on the photodegradation of 2,4-D by Au- BiFeO_3 , (b) zeta potential graph and (c) influence of catalyst loading on the photodegradation of 2,4-D by Au- BiFeO_3 .

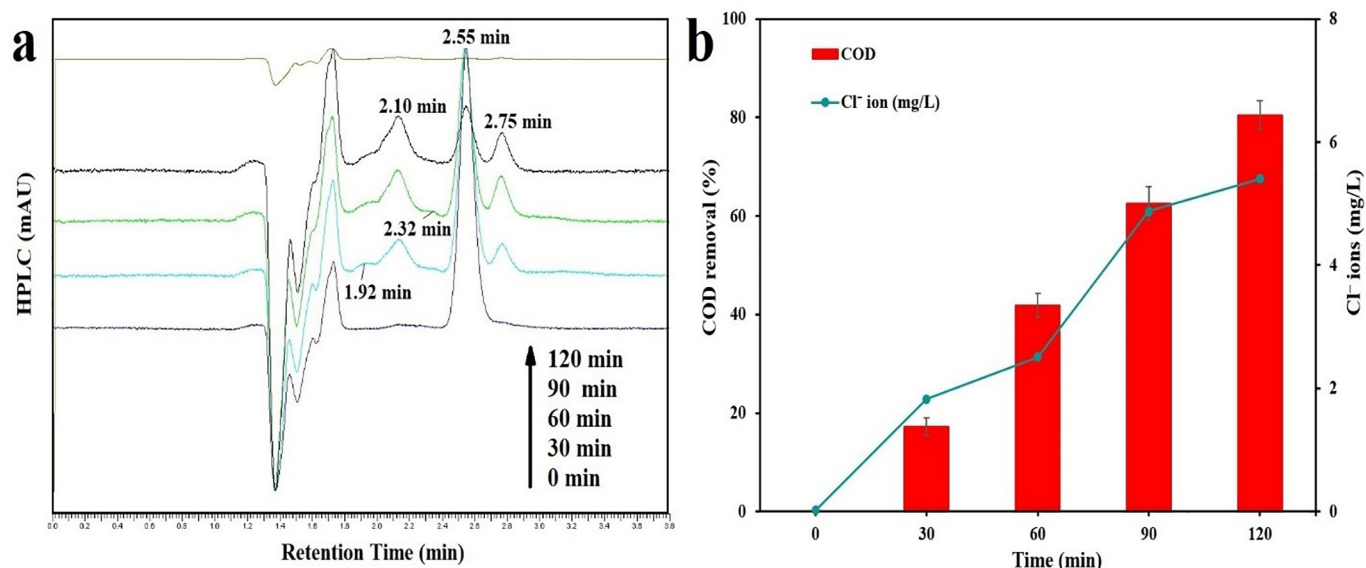


Fig. 8. (a) HPLC profiles for 2,4-D solution treated by the Au-BiFeO₃ composite at different irradiation times and (b) COD removal and chloride ion concentration of 2,4-D over Au-BiFeO₃ composite.

obtained data revealed that the treatment time needed for the mineralization process was relatively higher than the photodegradation of mother compound (120 min for 20 mg/L 2,4-D). This phenomenon explicated that 2,4-D produced numerous by-products prior to the completion of mineralization. Meanwhile, the concentration of free Cl⁻ ion formed during the photodegradation of 2,4-D was gradually increased along the treatment time and 5.4 mg/L Cl⁻ ion concentration was detected after the 120 min irradiation.

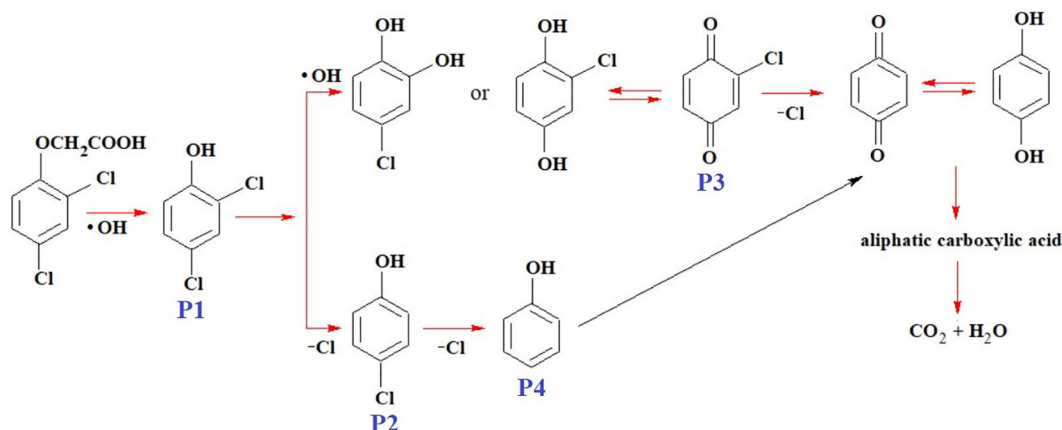
Based on the outcomes of the HPLC and corresponding chemical components produced upon the oxidation reaction (Fig. 8a and b), a plausible photodegradation pathway of 2,4-D over the Au-BiFeO₃ catalyst surface is postulated in Scheme 2. The photodegradation of 2,4-D was initiated by the rupturing of its side chain via the breakage of C—O bond to yield 2,4-dichlorophenol (2,4-DCP) (P1). These 2,4-DCP molecules can be dechlorinated to form 4-chlorophenol (4-CP) (P2) or oxidized to produce chlorohydroquinone or chlorobenzoquinone (CBQ) (P3). Both the 4-CP and CBQ molecules can then be converted to the phenol (P4) and BQ or hydroquinone, respectively via the dichlorination process. Thereafter, low molecular weight aliphatic carboxylic acids were produced from the cleavage of benzene rings of BQ or hydroquinone over the catalyst surface. Ultimately, these carboxylic

acids were mineralized to carbon dioxide, water and Cl⁻ ions as final products.

3.5. Enhancement behind 2,4-D photodegradation mechanism

3.5.1. Detection of ROS

The radical oxidative species (ROS) in the photodegradation process was assessed via various capturing agents. As can be observed in Fig. 9a, the photodegradation efficiency of 2,4-D did not change significantly when BQ was introduced, suggesting that •O₂⁻ radical contributed to a minor extent. Nonetheless, after adding IPA, KI and catalase, the photoactivity was dramatically decreased 2,4-D photodegradation to 27.6%, 34.9% and 29.2%, respectively, implying that •OH, h⁺ and H₂O₂ were the dominated ROS. This hypothesis can be further validated by electron spin resonance (ESR) analysis. Fig. 9b indicates that a strong typical signal of the DMPO•OH was witnessed in the presence of Au-BiFeO₃ composite after 5 min light irradiation and the signal intensity improved when extended the irradiation time. Nevertheless, no signal can be detected in dark condition. This data was corroborated with the outcomes of trapping experiments. These data confirmed that the



Scheme 2. Schematic representation of 2,4-D degradation pathway upon the photocatalytic reaction.

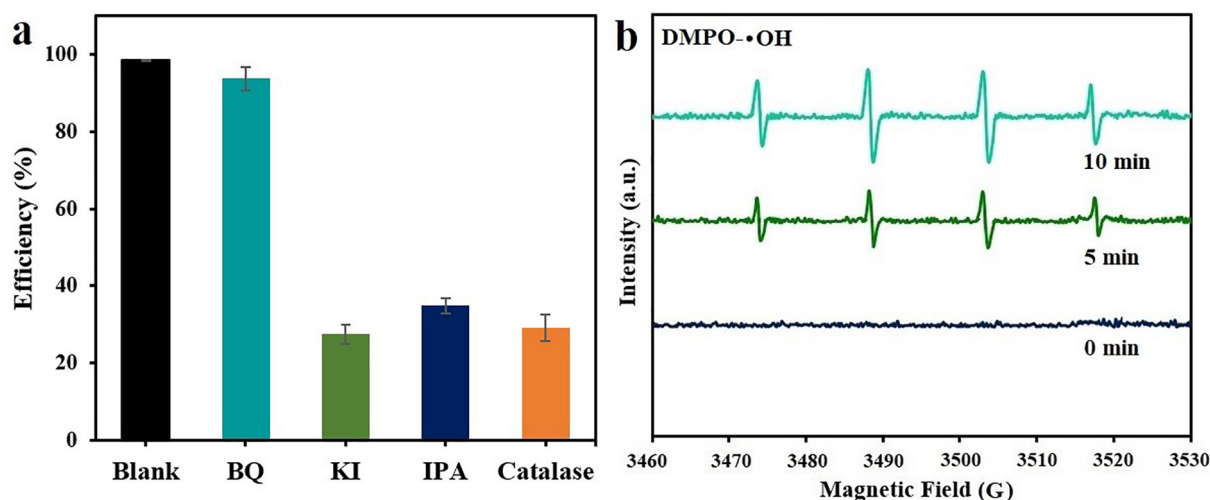


Fig. 9. (a) Radical trapping assessment of ROS during the 2,4-D photodegradation over Au-BiFeO₃ composite and (b) DMPO spin-trapping ESR spectra of Au-BiFeO₃ composite for DMPO-•OH.

Au-BiFeO₃ composite can boost the yield of •OH radicals and consequently participated in the 2,4-D photodegradation.

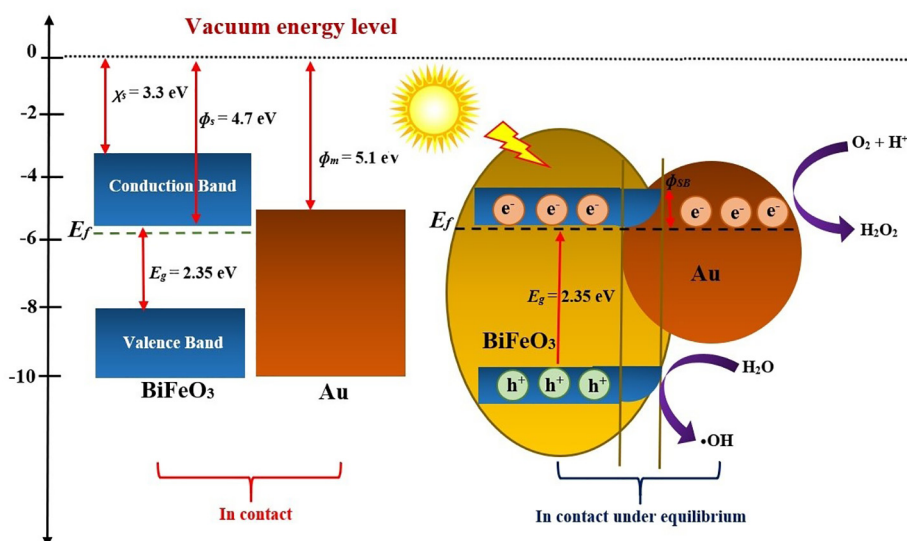
3.5.2. Reasonable photodegradation mechanism

According to the findings of aforementioned analyses, a reasonable 2,4-D photodegradation mechanism of Au-BiFeO₃ composite was put forward as depicted in Scheme 3. Under exposure of sunlight irradiation, the electron (e⁻) of BiFeO₃ were activated to its CB and subsequently left the primordial hole (h⁺) in the VB. For the bare BiFeO₃, the photogenerated charge carrier recombination rate was fast and only limited numbers of them could reach the catalyst surface, which resulted in low photoactivity. In contrast, decoration of Au on the coral-like BiFeO₃ surface can induce the energy band bending at the interface and a Schottky barrier (SB), which enabled the e⁻ capture at the heterojunction. This free e⁻ can transport between BiFeO₃ and Au because of the differences in their work functions. The Au had a higher work function (ϕ_m) of 5.1 eV [34,35] than that of the BiFeO₃ (ϕ_s) of 4.7 eV [36], which can facilitate the e⁻ migration from the CB of BiFeO₃ to the Au cocatalyst. Moreover, owing to the higher ϕ_m of Au

than that of BiFeO₃, the SB formed at the interface led to an upward band bending. The height of SB (ϕ_{SB}) can be determined using the following formula [37]:

$$\phi_{SB} = \phi_m - \chi_s \quad (4)$$

where ϕ_{SB} is the height of Schottky barrier, and χ_s (3.3 eV) is the electron affinity of BiFeO₃ [1]. The obtained ϕ_{SB} value was 1.8 eV and the energy band bending can decelerate the e⁻ transfer from BiFeO₃ to Au at equilibrium (Scheme 3b). Moreover, more photogenerated h⁺ can be accumulated at the interface and this condition improved the oxidizing ability and the generation of •OH radicals. Consequently, the Au cocatalyst can act as an effective cocatalyst in extending the lifetime of photogenerated charge carrier and hence boosted the photocatalytic performance of composite. For the 2,4-D photodegradation, on one hand, the photoexcited e⁻ in the Au-BiFeO₃ could be captured by O₂ molecules and H⁺ ions to form H₂O₂ because of the standard redox potential ($E^0(\text{O}_2/\text{H}_2\text{O}_2) = +0.695$ V vs. NHE) lower than CB edge potential (+0.29 eV) [38,39]. Meanwhile, the generated •OH by oxidizing OH⁻ or H₂O was due to the $E_0(\bullet\text{OH}/\text{OH}^-)$ (+1.99 eV vs. NHE) and $E_0(\bullet\text{OH}/\text{H}_2\text{O})$



Scheme 3. Schematic illustration of energy band mechanism of Au-BiFeO₃ composites in contact before and after equilibrium under sunlight exposure.

(+2.68 eV vs NHE) lower than the VB edge potential (+2.79 eV) [40]. The obtained H_2O_2 , h^+ , $\cdot\text{OH}$ radicals were then vigorously attack on the 2,4-D molecules and eventually converted into the mineralized products.

3.6. Magnetic property and cyclic degradation

Based on the earlier reports [5,6], BiFeO_3 is ferromagnetic at room temperature and the Au- BiFeO_3 composite might also displayed the ferromagnetic feature. Fig. 10 depicts the magnetic hysteresis (M-H) loops of the bare BiFeO_3 and Au- BiFeO_3 composite recorded at room temperature. The M-H loops of bare BiFeO_3 and Au- BiFeO_3 presented small hysteresis loops, which demonstrated that the samples have ferromagnetic features with the saturation magnetization (M_s) value of 4.80 emu/g and 3.95 emu/g, respectively. The low M_s value of Au- BiFeO_3 was due to the presence of non-magnetic Au nanoparticles decorated on the coral-like surfaces. Nevertheless, the Au- BiFeO_3 composite still possessed a higher M_s value than those of other reported magnetic-based composites [41–43]. The magnetic characteristic of the Au- BiFeO_3 composite can have practical applications. The magnetic separability of Au- BiFeO_3 was evaluated by applying a magnet bar closed to a flask-bearing the solid materials. The Au- BiFeO_3 was attracted to the magnet side within 15 min (inset of Fig. 10a).

The stability and reproducibility of the catalyst were studied over six cyclic runs. As presented in Fig. 10b, the photocatalytic performance of bare BiFeO_3 was significantly decreased from 50.0% to 32.6%, while the Au- BiFeO_3 composite was maintained well with slight declination

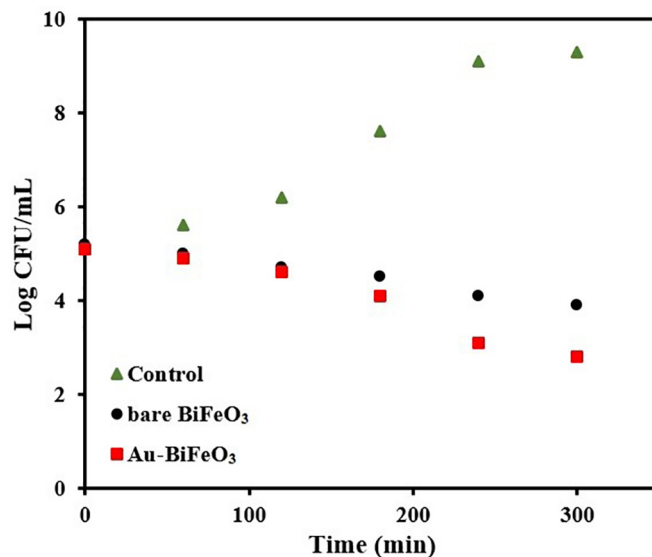


Fig. 11. Inactivation efficiency of the Au- BiFeO_3 composite against *E. coli* at different times.

around 89.6% after sixth cyclic run. In this study, the Fe^{3+} and Au^0 ions leakage throughout the cyclic degradation tests were also monitored using ICP-MS technique. No leakage of Fe^{3+} was found in the tests, while low concentrations of Au^0 ranged from 0.035 to

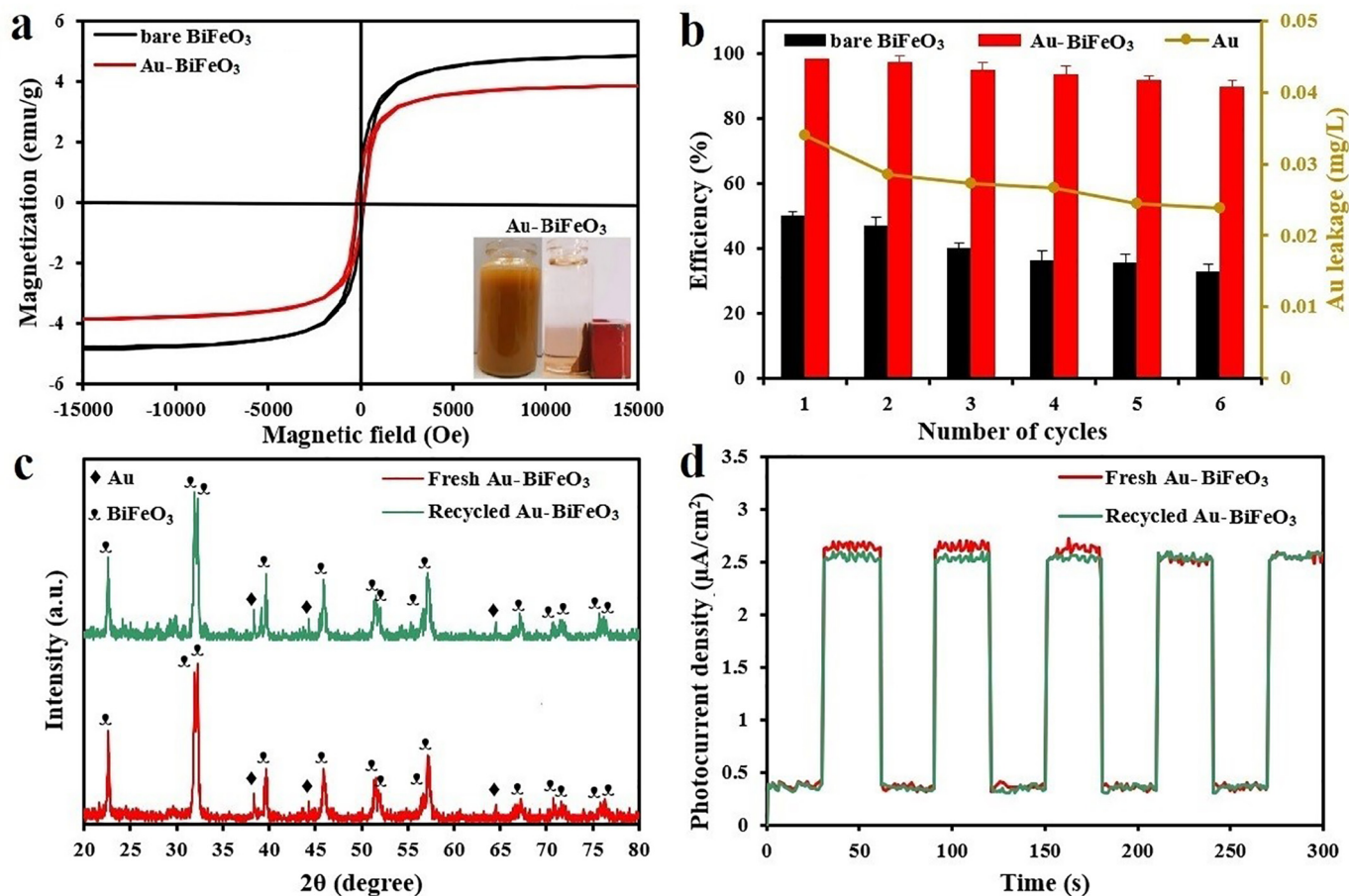


Fig. 10. (a) Magnetization curves of bare BiFeO_3 and Au- BiFeO_3 composite. (b) photodegradation of 2,4-D and Au leakage using bare BiFeO_3 and Au- BiFeO_3 composite over six cyclic runs, (c) XRD patterns of the fresh and used Au- BiFeO_3 composites and (d) transient photocurrent response of used Au- BiFeO_3 composite compared with the fresh one. Inset of (a) the image of magnetic separation for 15 min.

Table 1
Comparison of photocatalytic and antibacterial activities of various Au-decorated composite catalysts.

Composite catalyst	Magnetic	Light source	Pollutant and concentration	Removal efficiency	Microbe	Antibacterial efficiency	Ref.
Au-PdO/GO	×	100 W Hg lamp, $\lambda = 254$ nm	Tetrodotoxin	95% within 60 min under 0.15 mmol/L H ₂ O ₂	<i>E. coli</i> , <i>S. aureus</i> ,	99.5%	[49]
Au@ α -Fe ₂ O ₃	✓	Solar lamp	Rhodamine B, 10 mg/L	~88% within 60 min	<i>E. coli</i>	OD ₆₀₀ : 0.4490	[50]
Au@Fe ₂ O ₃	✓	100 W bulb	Methylene blue	94% within 50 min	<i>E. coli</i> , <i>B. subtilis</i>	ZOI*: 20, 18 mm	[51]
Au-TiO ₂	×	300 W Xe lamp, $\lambda = 420$ nm	Ciprofloxacin, 20 mg/L	84.1% within 240 min	<i>E. coli</i>	88.2% within 720 min	[52]
Ag-Au/ZnO	×	Solar light, 1250 × 100 lx	Acid red, 5×10^{-4} M	100% within 90 min	<i>B. subtilis</i> , <i>E. coli</i> , <i>P. aeruginosa</i> , <i>S. aureus</i> , <i>S. pyogenes</i>	ZOI*: 11, 12, 9, 12, 15 mm	[53]
Au-ZnO	×	2 × 8 W black UV lamps	Methylene blue, 2×10^{-5} M	25% within 160 min	<i>E. coli</i> , <i>S. aureus</i> , <i>E. ashbyii</i>	ZOI*: 4.3, 7.0, 9.75 mm	[54]
Au-BiFeO ₃	✓	Sunlight, 865.7 W/m ²	2,4-D, 20 mg/L	98.5% within 120 min	<i>E. coli</i>	56.0% within 300 min	Current study

* ZOI = Zone of inhibition.

0.024 mg/L was identified. However, these Au concentrations were still lower than the reported literatures [44–46]. Both fresh Au-BiFeO₃ and the composite after sixth cyclic run were assessed by XRD and transient photocurrent response. As indicated in Fig. 10c, no obvious change in the XRD diffraction peaks was observed after the cyclic degradation, implying that the phase composition and structure of the sample has not diminished. Besides, the transient photocurrent response on the used Au-BiFeO₃ composite was also monitored as illustrated in Fig. 10d. It can be observed that both the photocurrent density plots were highly similar over the six cyclic runs. This work indicated that the Au-BiFeO₃ composite had a good stability as well as highly feasible for continuous wastewater treatment.

3.7. Bactericidal effect

Fig. 11 shows the bactericidal effect of the Au-BiFeO₃ along with bare BiFeO₃ and control (absent of composite). Au-BiFeO₃ has a better bactericidal effect than that of bare BiFeO₃. On the contrary, no significant inactivation of *E. coli* cell was happened on the control experiment. It can be observed that the Au-BiFeO₃ possessed a strong bactericidal effect which should stem from the effective charge carrier separation and transportation processes in the Au-BiFeO₃ during the sunlight exposure. The interaction between the Au-BiFeO₃ heterostructure and bacteria gave rise to the membrane integrity leakages, like cytoplasm, potassium ion, DNA and ribosome molecules owing to the ROS attack on the bacterial species surface, which led to the enhancement of bacterial inactivation [47,48]. In the actual wastewater treatment, microorganism contamination can greatly restrain the photocatalysis efficiency. Such a high antibacterial capability of the Au-BiFeO₃ composite can avoid it from being polluted by the microorganisms, which were highly conducive for the viability of this catalyst in the actual wastewater purification application.

The photocatalytic capacity comparison with the present Au-BiFeO₃ and different kinds of Au-based composites cited from references are provided in Table 1. It was difficult to quantitatively compare the photoactivities with previous reported systems because of the various experimental conditions for photocatalytic process. For instance, the operational parameters of catalyst loading, degraded contaminants, light source, duration of treatment and etc. greatly affected the photodegradation. Nonetheless, it can still be observed that the magnetic-based catalyst prepared in this work had excellent photocatalytic and antibacterial activities.

4. Conclusion

By adjusting the loadings of Au, Au-BiFeO₃ composite have been successfully fabricated by facile two-steps facile hydrothermal technique. The as-fabricated catalyst was analyzed through instrumentation

techniques to check on the morphological, structural, optical, electronic and magnetic traits of the catalyst. Compared to bare BiFeO₃, the Au-BiFeO₃ composite exhibited a pronounced sunlight-responsive photoactivities for the 2,4-D degradation and *E. coli* inactivation. The Au nanoparticles dispersed on the coral-like BiFeO₃ structure can afford more photocatalytic active sites, facilitated the h⁺ accumulation at the interface and further enhanced oxidizing ability as well as the formation of •OH radicals. In-depth PL and electronic investigations also concluded the remarkable photocatalytic performance. The possible photocatalytic mechanism was elucidated and supported with the data according to the radical trapping and ESR experiments. Additionally, intermediates identification results evidently indicated the 2,4-D decomposition effect. The Au-BiFeO₃ can be easily recovered via an external magnet and demonstrated great reusability with a minimal leakage of Au after six runs. This work offers the viable and tantalizing prospective of utilizing the noble metal-based magnetic catalyst in the multifunctional photocatalytic areas.

Declaration of Competing Interest

None.

Acknowledgments

This research was supported by Ministry of Higher Education (MoHE) through Fundamental Research Grant Scheme (FRGS/1/2019/TK02/UTAR/02/4), Universiti Tunku Abdul Rahman (UTARRF/2020-C1/S04 and UTARRF/2020-C2/L02), Research Funds of The Guangxi Key Laboratory of Theory and Technology for Environmental Pollution Control, China (1801K012 and 1801K013), ASEAN Young Talented Scientist Program of Guangxi and special funding for Guangxi “Bagui Scholar” construction project.

References

- [1] M.W. Kee, J.W. Soo, S.M. Lam, J.C. Sin, A.R. Mohamed AR, Evaluation of photocatalytic fuel cell (PFC) for electricity production and simultaneous degradation of methyl green in synthetic and real greywater effluents, *J. Environ. Manag.* 228 (2018) 383–392.
- [2] M. Ahmad, I. Ahmad, E. Ahmed, M.S. Akhtar, N.R. Khalid, Facile and inexpensive synthesis of Ag doped ZnO/CNTs composite: study on the efficient photocatalytic activity and photocatalytic mechanism, *J. Mol. Liq.* 311 (2020) 113326.
- [3] S.M. Lam, J.C. Sin, A.Z. Abdullah, A.R. Mohamed, Photocatalytic degradation of resorcinol - an endocrine disrupter, by TiO₂ and ZnO suspensions, *Environ. Technol.* 34 (2013) 1097–1106.
- [4] D.M. Han, W.P. Jia, H.D. Liang, Selective removal of 2,4-dichlorophenoxyacetic acid from water by molecularly-imprinted amino-functionalized silica gel sorbent, *J. Environ. Sci.* 22 (2010) 237–241.
- [5] S.M. Lam, J.C. Sin, A.R. Mohamed, A newly emerging visible light-responsive BiFeO₃ perovskite for photocatalytic applications: A mini review, *Mater. Res. Bull.* 90 (2017) 15–30.

- [6] C. Ponraj, G. Vinitha, J. Daniel, A review on the visible light active BiFeO₃ nanostructures as suitable photocatalyst in the degradation of different textile dyes, *Environ. Nanotechnol. Monit. Manag.* 7 (2017) 110–120.
- [7] M. Sakar, S. Balakumar, P. Saravanan, S.N. Jaisankar, Electric field induced formation of one-dimensional bismuth ferrite (BiFeO₃) nanostructures in electrospinning process, *Mater. Des.* 94 (2016) 487–495.
- [8] X. Zhang, B. Wang, X. Wang, X. Xiao, Z. Dai, W. Wu, J. Zheng, F. Ren, C. Jiang, Preparation of M@BiFeO₃ nanocomposites (M = Ag, Au) bowl arrays with enhanced visible light photocatalytic activity, *J. Am. Ceram. Soc.* 98 (2015) 2255–2263.
- [9] G.S. Lotey, N.K. Verma, Synthesis and characterization of BiFeO₃ nanowires and their applications in dye-sensitized solar cells, *Mater. Sci. Semicond. Process.* 21 (2014) 206–211.
- [10] C. Hao, J. Xiang, H. Hou, W. Lv, Y. Lv, W. Hu, Photocatalytic performances of BiFeO₃ particles with the average size in nanometer, submicrometer and micrometer, *Mater. Res. Bull.* 50 (2014) 369–373.
- [11] B. Zhou, Y. Li, J. Bai, X. Li, F. Li, L. Liu, Controlled synthesis of rh-In₂O₃ nanostructures with different morphologies for efficient photocatalytic degradation of oxytetracycline, *Appl. Surf. Sci.* 464 (2019) 115–124.
- [12] M. Karmaoui, L. Lajaunie, D.M. Tobaldi, G. Leonardi, C. Benbayer, R. Arenal, J.A. Labrincha, G.N. School, Modification of anatase using noble-metals (Au, Pt, Ag): toward a nanoheterojunction exhibiting simultaneously photocatalytic activity and plasmonic gas sensing, *Appl. Catal. B Environ.* 218 (2017) 370–384.
- [13] B. Amanulla, S. Sannasi, A.K.M. Abubakker, S.K. Ramaraj, A magnetically recoverable bimetallic Au-FeNPs decorated on g-C₃N₄ for efficient photocatalytic degradation of organic contaminants, *J. Mol. Liq.* 249 (2018) 754–763.
- [14] Z. Ebrahimpour, N. Mansour, Plasmonic near-field effect on visible and near-infrared emissions from self-assembled gold nanoparticle films, *Plasmonics* 13 (2018) 1335–1342.
- [15] S.M. Lam, J.A. Quek, J.C. Sin, Mechanistic investigation of visible light responsive Ag/ZnO micro/nanoflowers for enhanced photocatalytic performance and antibacterial activity, *J. Photochem. Photobiol. A: Chem.* 353 (2018) 171–185.
- [16] F. Niu, D. Chen, L. Qin, T. Gao, N. Zhang, S. Wang, Z. Chen, J. Wang, X. Sun, Y. Huang, Synthesis of Pt/BiFeO₃ heterostructured photocatalysts for highly efficient visible-light photocatalytic performances, *Sol. Energy Mater. Sol. Cells* 143 (2015) 386–396.
- [17] J. Bi, Z. Zhou, M. Chen, S. Liang, Y. He, Z. Zhang, L. Wu, Plasmonic Au/CdMoO₄ photocatalyst: influence of surface plasmon resonance for selective photocatalytic oxidation of benzylic alcohol, *Appl. Surf. Sci.* 349 (2015) 292–298.
- [18] A.M. Mostafa, S.A. Yousef, W.H. Eisa, M.A. Ewaida, E.A. Al-Ashkar, Au@CdO core/shell nanoparticles synthesized by pulsed laser ablation in Au precursor solution, *Appl. Phys. A Mater. Sci. Process.* 123 (2017) 774.
- [19] X. Liu, Y. Su, J. Lang, Z. Chai, X. Wang, A novel Au-loaded Na₂Ta₂O₆ multifunctional catalyst: Thermocatalytic and photocatalytic elimination of the poisonous nitrobenzene derivatives from wastewater under natural condition, *J. Alloys Compd.* 695 (2017) 60–69.
- [20] S. Verma, B.T. Rao, J. Jayabalan, S.K. Rai, D.M. Phase, A.K. Srivastava, R. Kaul, Studies on growth of Au cube-ZnO core-shell nanoparticles for photocatalytic degradation of methylene blue and methyl orange dyes in aqueous media and in presence of different scavengers, *J. Environ. Chem. Eng.* 7 (2019) 103209.
- [21] F. Niu, D. Chen, L. Qin, N. Zhang, J. Wang, Z. Chen, Y. Huang, Facile synthesis of highly efficient p-n heterojunction CuO/BiFeO₃ composite photocatalysts with enhanced visible-light photocatalytic activity, *ChemCatChem* 7 (2015) 3279–3289.
- [22] T. Yamashita, P. Hayes, Analysis of XPS spectra of Fe²⁺ and Fe³⁺ ions in oxide materials, *Appl. Surf. Sci.* 254 (2008) 2441–2449.
- [23] S. Bharathkumar, M. Sakar, R.V. K. S. Balakumar, Versatility of electrospinning in the fabrication of fibrous mat and mesh nanostructures of bismuth ferrite (BiFeO₃) and their magnetic and photocatalytic activities, *Phys. Chem. Chem. Phys.* 17 (2015) 17745–17754.
- [24] S.M. Lam, J.C. Sin, H. Lin, H.X. Li, J.W. Lim, H.H. Zeng, A Z-scheme WO₃ loaded-hexagonal rod-like ZnO/Zn photocatalytic fuel cell for chemical energy recuperation from food wastewater treatment, *Appl. Surf. Sci.* 514 (2020) 145945.
- [25] T. Fan, C. Chen, Z. Tang, Y. Ni, C. Lu, Synthesis and characterization of g-C₃N₄/BiFeO₃ composites with an enhanced visible light photocatalytic activity, *Mater. Sci. Semicond. Process.* 40 (2015) 439–445.
- [26] K. Saravanakumar, R. Karthik, S.-M. Chen, J.V. Kumar, K. Prakash, V. Muthuraj, Construction of novel Pd/CeO₂/g-C₃N₄ nanocomposites as efficient visible-light photocatalysts for hexavalent chromium detoxification, *J. Colloid Interface Sci.* 504 (2017) 514–526.
- [27] R.G. Pearson, Absolute electronegativity and hardness: application to inorganic chemistry, *Inorg. Chem.* 27 (1988) 734–740.
- [28] J.C. Sin, S.M. Lam, H.H. Zeng, H. Lin, H.X. Li, A.K. Kumaresan, A.R. Mohamed, J.W. Lim, Z-scheme heterojunction nanocomposite fabricated by decorating magnetic MnFe₂O₄ nanoparticles on BiOBr nanosheets for enhanced visible light photocatalytic degradation of 2,4-dichlorophenoxyacetic acid and Rhodamine B, *Sep. Purif. Technol.* 250 (2020) 117186.
- [29] C.Z. Wang, X.D. Shao, J. Pan, J.G. Hu, X.Y. Xu, Redox bifunctional activities with optical gain of Ni₃S₂ nanosheets edged with MoS₂ for overall water splitting, *Appl. Catal. B Environ.* 268 (2020) 118435.
- [30] S. Jin, X.X. Ma, J. Pan, C.Y. Zhu, S.E. Saji, J.G. Hu, X.Y. Xu, L.T. Sun, Z.Y. Yin, Oxygen vacancies activating surface reactivity to favor charge separation and transfer in nanoporous BiVO₄ photoanode, *Appl. Catal. B Environ.* 281 (2021) 119477.
- [31] A. Zhang, J. Zhang, Characterization and photocatalytic properties of Au/BiVO₄ composites, *J. Alloys Compd.* 491 (2010) 631–635.
- [32] Z. Mo, H. Xu, Z. Chen, X. She, Y. Song, P. Yan, Y. Xu, Y. Lei, S. Yuan, H. Li, Gold/monolayer graphitic carbon nitride plasmonic photocatalyst for ultrafast electron transfer in solar-to-hydrogen energy conversion, *Chin. J. Catal.* 39 (2018) 760–770.
- [33] B. Babu, R. Koutavarapu, V.V.N. Harish, J. Shim, K. Yoo, Novel in-situ synthesis of Au/SnO₂ quantum dots for enhanced visible-light-driven photocatalytic applications, *Ceram. Int.* 45 (2019) 5743–5750.
- [34] Y. Cheng, W. Wang, L. Yao, J. Wang, Y. Liang, J. Fu, Insights into charge transfer and solar light photocatalytic activity induced by the synergistic effect of defect state and plasmon in Au nanoparticle-decorated hierarchical 3D porous ZnO microspheres, *Appl. Surf. Sci.* 494 (2019) 959–968.
- [35] X. Zheng, Z. Zhang, S. Meng, Y. Wang, D. Li, Regulating charge transfer over 3D Au/ZnO hybrid inverse opal toward efficiently photocatalytic degradation of bisphenol A and photoelectrochemical water splitting, *Chem. Eng. J.* 393 (2020) 124676.
- [36] M. Liu, H. Zhu, Y. Zhang, C. Xue, J. Ouyang, Energy storage characteristics of BiFeO₃/BaTiO₃ Bi-layers integrated on Si, *Materials* 9 (2016) 935.
- [37] M. Guy, Ozacar Nuray, The influence of noble metals on photocatalytic activity of ZnO for Congo red degradation, *Int. J. Hydrog. Energy* 41 (2016) 20100–20112.
- [38] S. Chaiwichian, K. Wetchakun, W. Kangwansupamonkon, N. Wetchakun, Novel visible-light-driven BiFeO₃-Bi₂WO₆ nanocomposites toward degradation of dyes, *J. Photochem. Photobiol. A Chem.* 349 (2017) 183–192.
- [39] L. Di, H. Yang, T. Xian, X. Chen, Enhanced photocatalytic degradation activity of BiFeO₃ microspheres by decoration with g-C₃N₄ nanoparticles, *Mater. Res.* 21 (2018) 1–10.
- [40] Y. Chen, P. Zhu, M. Duan, J. Li, Z. Ren, P. Wang, Fabrication of a magnetically separable and dual Z-scheme PANI/Ag₃PO₄/NiFe₂O₄ composite with enhanced visible-light photocatalytic activity for organic pollutant elimination, *Appl. Surf. Sci.* 486 (2019) 198–211.
- [41] S. Cheng, Q. Xu, X. Hao, Z. Wang, N. Ma, P. Du, Formation of nano-Ag/BiFeO₃ composite thin film with extraordinary high dielectric and effective ferromagnetic properties, *J. Mater. Sci. Mater. Electron.* 28 (2017) 5652–5662.
- [42] L. Gong, Z. Zhou, S. Wang, B. Wang, Preparation and characterization of BiFeO₃@Ce-doped TiO₂ core-shell structured nanocomposites, *Mater. Sci. Semicond. Process.* 16 (2013) 288–294.
- [43] P.C. Sati, M. Kumar, S. Chhoker, Raman spectroscopy and enhanced magnetic and dielectric properties of Pr and Ti codoped BiFeO₃ ceramics, *J. Mater. Sci. Mater. Electron.* 26 (2015) 530–538.
- [44] B.K. Min, J.E. Heo, N.K. Youn, O.S. Joo, H. Lee, J.H. Kim, H.S. Kim, Tuning of the photocatalytic 1, 4-dioxane degradation with surface plasmon resonance of gold nanoparticles on titania, *Catal. Commun.* 10 (2009) 712–715.
- [45] M.M. Khan, S.A. Ansari, M.E. Khan, M.O. Ansari, B.-K. Min, M.H. Cho, Visible light-induced enhanced photoelectrochemical and photocatalytic studies of gold decorated SnO₂ nanostructures, *New J. Chem.* 39 (2015) 2758–2766.
- [46] Z. Bian, J. Zhu, F. Cao, Y. Lu, H. Li, In situ encapsulation of Au nanoparticles in mesoporous core-shell TiO₂ microspheres with enhanced activity and durability, *Chem. Commun.* (2009) 3789–3791.
- [47] J.A. Quek, S.M. Lam, J.C. Sin, A.R. Mohamed, Visible light responsive flower-like ZnO in photocatalytic antibacterial mechanism towards *Enterococcus faecalis* and *Micrococcus luteus*, *J. Photochem. Photobiol. B Biol.* 187 (2018) 66–75.
- [48] K.A. Wong, S.M. Lam, J.C. Sin, Wet chemically synthesized ZnO structures for photodegradation of pre-treated palm oil mill effluent and antibacterial activity, *Ceram. Int.* 45 (2019) 1868–1880.
- [49] A. Fakhri, M. Naji, Degradation photocatalysis of tetrodotoxin as a poison by gold doped PdO nanoparticles supported on reduced graphene oxide nanocomposites and evaluation of its antibacterial activity, *J. Photochem. Photobiol. B Biol.* 167 (2017) 58–63.
- [50] E. Alp, R. Imamoglu, U. Savaci, S. Turan, M.K. Kazmanli, A. Genç, Plasmon-enhanced photocatalytic and antibacterial activity of gold nanoparticles-decorated hematite nanostructures, *J. Alloys Compd.* 852 (2021) 157021.
- [51] S. Shams, A.U. Khan, Q.P. Yuan, W. Ahmad, Y. Wei, Z.U.H. Khan, S. Shams, A. Ahmad, A.U. Rahman, S. Ullah, Facile and eco-benign synthesis of Au@Fe₂O₃ nanocomposite: efficient photocatalytic, antibacterial and antioxidant agent, *J. Photochem. Photobiol. B Biol.* 199 (2019) 111632.
- [52] Y.N. Tang, H. Sun, Y.X. Shang, S. Zeng, Z. Qin, S.Y. Yin, J.Y. Li, S. Liang, G.L. Lu, Z.N. Liu, Spiky nanohybrids of titanium dioxide/gold nanoparticles for enhanced photocatalytic degradation and anti-bacterial property, *J. Colloid Interface Sci.* 535 (2019) 516–523.
- [53] A. Senthilraja, B. Krishnakumar, R. Hariharan, A.J.F.N. Sobral, C. Suryad, N. Agnel, A. John, M. Shanthia, Synthesis and characterization of bimetallic nanocomposite and its photocatalytic, antifungal and antibacterial activity, *Sep. Purif. Technol.* 202 (2018) 373–384.
- [54] T.K. Pathak, R.E. Kroona, H.C. Swart, Photocatalytic and biological applications of Ag and Au doped ZnO nanomaterial synthesized by combustion, *Vacuum* 157 (2018) 508–513.